



# UNIVERSITÀ DEGLI STUDI DI TORINO

***This is an author version of the contribution published on:***

Umili, G., Ferrero, A., & Einstein, H. H. (2013). A new method for automatic discontinuity traces sampling on rock mass 3D model. *Computers and Geosciences*, Volume 51, February 2013, Pages 182-192  
**DOI:** 10.1016/j.cageo.2012.07.026.

***The definitive version is available at:***

*La versione definitiva è disponibile alla URL:*

[http://ac.els-cdn.com/S0098300412002695/1-s2.0-S0098300412002695-main.pdf?\\_tid=fbcb6b396-aa86-11e3-b387-00000aacb35d&acdnat=1394698427\\_2d7ab4d587ccb74e8eae864379f09fd9](http://ac.els-cdn.com/S0098300412002695/1-s2.0-S0098300412002695-main.pdf?_tid=fbcb6b396-aa86-11e3-b387-00000aacb35d&acdnat=1394698427_2d7ab4d587ccb74e8eae864379f09fd9)

## **A new method for automatic discontinuity traces sampling on rock mass 3D model**

**Umili G.<sup>(a)</sup>, Ferrero A.<sup>(a)</sup>, Einstein H.H.<sup>(b)</sup>**

<sup>(a)</sup> Department of Civil, Environmental and Territory Engineering, University of Parma, Viale G.P. Usberti, 181/A

43124 Parma, Italy. gessica.umili@nemo.unipr.it, annamaria.ferrero@unipr.it

<sup>(b)</sup> Department of Civil and Environmental Engineering, Massachusetts Institute of Technology, 77 Massachusetts Avenue, Cambridge,

MA 02139, USA. einstein@mit.edu

Corresponding author:

Gessica Umili

Department of Civil, Environmental and Territory Engineering, University of Parma, Viale G.P. Usberti, 181/A

43124 Parma, Italy.

e-mail: gessica.umili@nemo.unipr.it

telephone: +39 0521 906055

fax: +39 0521 905924

### **ABSTRACT:**

A new automatic method for discontinuity traces mapping and sampling on a rock mass digital model is described in this work. The implemented procedure allows one to automatically identify discontinuity traces on a Digital Surface Model: traces are detected directly as surface breaklines, by means of maximum and minimum principal curvature values of the vertices that constitute the model surface. Color influence and user errors, that usually characterize the trace mapping on images, are eliminated. Also trace sampling procedures based on circular windows and circular scanlines have been implemented: they are used to infer trace data and to calculate values of mean trace length, expected

discontinuity diameter and intensity of rock discontinuities. The method is tested on a case study: results obtained applying the automatic procedure on the DSM of a rock face are compared to those obtained performing a manual sampling on the orthophotograph of the same rock face.

**Keywords:** automatic, trace mapping, rock mass, 3D, curvature, edge.

## 1. Introduction

One of the fundamental parameters to characterize a rock mass is discontinuity persistence, defined as the ratio between the total discontinuity area and a reference area (surface); direct measurements of discontinuity area are quite impossible to obtain, and therefore another discontinuity feature is used to infer discontinuity area and this is the discontinuity trace. The trace can be defined as the intersection between the discontinuity and the outcrop surface. Thus an easier way to obtain a persistence is to measure discontinuity traces and to relate these data to the real persistence, even if it must be remarked that “the relation between discontinuity extent and the produced traces is unavoidably probabilistic“(Dershowitz, 1979). The traditional discontinuity sampling procedure consists of a manual survey performed by an operator directly on the rock mass (ISRM, 1978); this approach allows one to obtain data concerning discontinuity orientation, aperture, roughness, spacing and also about trace lengths. However, issues related to the duration of the procedure, to the operator’s safety during the survey and to direct access problems lead many authors to propose non-contact methods, namely, procedures which allow one to perform the trace survey on a representation of the rock mass, such as an image or a digital model.

Automatic or semi-automatic methods for discontinuity traces identification on images have been proposed by many authors (e.g. Reid and Harrison, 2000; Post et al., 2001; Lemy and Hadjigeorgiou, 2003), showing the advantage of a non-contact approach; however, these methods suffer from common

issues related to the bidimensional nature of the representation. In fact, depending on the camera asset (defined by 3 angles, relative to the axes of the reference system) and position in relation to the rock mass surface (e.g. at the top or at the foot of the rock face), some orientations could be disadvantaged during the identification. For example a trace orthogonal to the image plane could be almost invisible and, in general, traces that are not parallel to the image plane could suffer from a significant perspective effect. Moreover, an image can contain occlusions: they are defined as a rock mass portion that, with respect to the camera asset and position, cannot be seen because it is hidden by a rock protrusion, so not all the rock mass surface will be available for the trace sampling. In addition, since traces identification is based on color data contained in the image, it must be considered that light in an uncontrolled environment can significantly vary, locally and globally, depending on exposition, weather conditions, rock type, etc. So different light conditions could lead to very different results.

Automatic or semi-automatic methods for discontinuity planes identification on digital models have been also proposed (Roncella and Forlani, 2005; Slob et al., 2007; Gigli and Casagli, 2011): these methods are based on the segmentation of the surface, and traces are obtained as the boundaries of the identified planes.

Once traces are identified with a contact or non-contact method, a sampling method must be used to infer data: it is possible to sample the traces (a) that intersect a line (*scanline*); (b) that intersect a circle (circular scanline) (Mauldon et al., 2001); or (c) within a finite size area, usually rectangular or circular in shape (*window*) (Kulatilake and Wu, 1984; Zhang and Einstein, 1998; Mauldon, 1998). Circular scanlines are simply circles drawn on a rock surface, on a fracture trace map or on a digital image. A circular window is the region enclosed by a circular scanline (Rohrbaugh et al., 2002).

The sampling procedure usually involves mapping the fracture pattern on a surface and recording characteristics of visible fractures (Wu and Pollard, 1995). Trace maps also have the advantage of

recording the trace pattern, termination relationships and other aggregate properties of the areal sample (Dershowitz and Einstein, 1988). Construction of fracture trace maps for areal samples, however, tends to be very time consuming (Rohrbaugh et al., 2002).

In this paper a new method to automatically identify discontinuity traces on a Digital Surface Model is presented: traces are detected directly as surface breaklines, by means of principal curvature values of the vertices that constitute the model surface. The method will be applied to a case study; then sampling methods proposed by Zhang and Einstein (1998) and Mauldon et al. (2001) will be used to infer trace data and to calculate values of mean trace length.

## **2. Methods for trace mapping**

Discontinuities are an intrinsic characteristic of rock masses and they appear at every scale of a technical survey. However, measurements tend to affect samples in favor of those structures which are privileged by observation procedures (Cravero and Iabichino, 1992). If one chooses to map traces directly on the rock mass, the identification procedure is quite easy, but the area that can be reasonably mapped will be small, mostly because the survey is very time-consuming and also because direct access to the rock mass is often difficult for the operator. If one chooses, instead, to perform the mapping on a bidimensional representation of the rock mass, such as an image, manual or automatic procedures can be safely performed without need for a direct access. However, trace detection on images can be a long and complex operation; in fact, the manual operation is time consuming and an expert operator is needed. Mapping performed by means of edge detection algorithms (Barrow and Tenenbaum, 1981; Canny, 1986; Lindeberg, 2001; Kemeny and Post, 2003) or segmentation techniques (Maerz, 1990; Reid and Harrison, 2000; Lemy and Hadjigeorgiou, 2003) are faster but results could be very complex and a manual editing phase could be needed. Moreover, light conditions could strongly influence the results' completeness and accuracy because of two effects: variations of

illumination and variations of reflectance. The first is due to weather conditions (e.g. presence or absence of cloud cover) and to the sun position with respect to the rock mass; the second is due to the rock type, color and conditions (e.g. wet rock) (Reid and Harrison, 2000). So with a 2D approach the area that can be reasonably mapped could be large, but the percentage of traces that can be identified among the true number of traces could vary significantly.

The issues discussed above led the authors to consider a new mapping method, which could combine the safety and the efficiency of a non-contact method, with the possibility to obtain a complete representation of the rock mass such as a digital 3D model. Therefore, an automatic procedure was developed to identify and to map discontinuity traces on a Digital Surface Model (DSM), which consists of a triangulated point cloud that approximates the true surface; it can be created with both photogrammetric techniques or laser scanner surveys and many authors discussed the advantages of such a procedure for rock mechanics purposes (Kemeny and Donovan, 2005; Roncella and Forlani, 2005; Trinks et al., 2005; Feng and Roshoff, 2006; Haneberg, 2006; Sturzenegger and Stead, 2009; Lato et al., 2012).

The proposed approach focuses on the geometrical definition of traces. As discussed before, a discontinuity trace is the intersection between the discontinuity plane and the outcrop surface. While most of the authors developed semi-automatic or automatic methods to extract discontinuity planes from a DSM (Slob et al., 2007; Ferrero et al., 2009; Gigli and Casagli, 2011), consider traces only as borders of these planes, this new method allows one to directly detect and map traces without extracting planes.

### **3. The new trace mapping method**

Natural outcrops can have an infinite variety of shapes and their dimensions can be very different, but a common characteristic is their non-planar surface. In fact, generally the surface has edges, that can be both asperities or depressions, most of them created by the intersections of different discontinuity planes. Therefore, the method presented here is based on the assumption that a discontinuity trace can be geometrically identified as an edge of the surface. This assumption is generally valid in natural outcrops, while on tunnel surfaces or other artificially profiled rock faces its validity could significantly decrease. This method allows one to detect traces created by the intersection of different visible planes, i.e. edges that are asperities or depressions of the DSM surface (Figure 1). So the quality of the DSM is fundamental (Kraus, 1993; Kraus and Pfeifer, 1998; Baltsavias, 1999): it can be evaluated in terms of resolution, i.e. the value of the mean distance between adjacent vertices. A higher resolution means that the mean distance between vertices is small, and that the correspondence between the discretized surface (DSM) and the actual rock mass surface (Figure 2) is improved. Therefore, the method generally allows one to detect traces whose surface dimensions are larger than the resolution. Also the dispersion (*noise*) of points relative to the theoretical surface influences the quality: the smaller the noise, the greater the quality.

The edge detection procedure presented here is based on the classification of each vertex of the model surface according to its principal curvature values; in fact asperities and depressions are composed of convex or concave surface portions, i.e. a certain number of triangulated vertices. So principal curvature is a good parameter to “measure” the vertices' convexity and concavity and, combined with principal curvature directions, it can be used to reconstruct paths (edges) that connect vertices along asperities and depressions.

Figure 1: Detail of a shaded surface portion of a Digital Surface Model (DSM), representing discontinuity planes separated by convex and concave edges.

Figure 2: Triangulated vertices which constitute portion of DSM in Fig.1; a) high resolution DSM produces a better representation of edges than b) low resolution.

In the following a concise definition of principal curvature and a brief description of the edge detection method applied to a DSM are given. For a detailed description of the algorithms see Umili (2011); a test-object called *stairs* will be used to explain the procedure (Figure 3); edges are straight and their paths follow one of the three axes X,Y,Z.

Figure 3: Example of convex and concave edges detected on test-object: DSM stairs is composed by 116601 points and 231909 triangles.

Considering a vertex P of a surface (Figure 4) and its normal N, it is possible to define the normal plane  $\pi$ , which contains P and N and cuts the surface generating a curve C which, among all possible curves, has the minimum osculating circle radius  $r$  in P (Euler, 1760). The smaller is the osculating circle radius, the faster is the slope variation of the surface and the higher is the absolute value of the normal curvature. Normal curvature is positive if the osculating circle is on the same side of the surface as N with respect to P, otherwise it is negative. It is therefore possible to define the Maximum Principal Curvature ( $k_{max}$ ) of P as the maximum value of normal curvature of C (convexity). Correspondingly, the Minimum Principal Curvature ( $k_{min}$ ) of P is the minimum value of normal curvature of C and it describes the concavity of the local surface.

Figure 4: Definition of principal curvature of a vertex P of a surface requires definition of normal N and normal plane  $\pi$ . a) Plane  $\pi_1$  generates a curve  $C_1$  whose osculating circle in P has a radius  $r_1$ ; b) plane  $\pi_2$  is obtained rotating  $\pi_1$  about the normal N; it generates a curve  $C_2$  whose osculating circle in P has a radius  $r_2$  greater than  $r_1$ .



The first step of the procedure is therefore the curvature calculation for each vertex of the DSM: the method proposed by Chen and Schmitt (1992) and extended by Dong and Wang (2005) is used. This method is accurate and requires one to solve only simple equations; as suggested by Dong and Wang (2005), it has been applied considering a two-ring neighborhood around each vertex to calculate the normal ( $N$ ). A one-ring neighborhood of vertex  $P$  is formed by all the triangles that contain  $P$  (Figure 5a); a two-ring neighborhood of  $P$  is formed by all the one-ring triangles and all the triangles that contain at least 1 vertex belonging to the one-ring neighborhood (Figure 5b).

Figure 5: a) One-ring neighborhood of vertex  $P$  is formed by all the triangles that contain  $P$ ; b) two-ring neighborhood of  $P$  is composed by one-ring triangles and triangles that contain at least 1 vertex belonging to one-ring neighborhood.

The normal  $N_t$  of a triangle is calculated as the normal of the plane containing the triangle. The normal  $N$  of vertex  $P$  is then calculated as the weighted mean of all the normals  $N_t$  of its two-ring neighborhood, in which weights consist of the inverse distances between  $P$  and the triangle centroids.

Since a greater convexity is characterized by a greater positive value of maximum principal curvature, while a greater concavity is characterized by a greater absolute value of minimum principal curvature and a negative sign, it is possible to identify paths that connect vertices with similar curvature values: in particular maximum  $k_{max}$  values identify convex edges (Figure 6a), while minimum  $k_{min}$  values identify concave edges (Figure 6b). Therefore the algorithms detect discontinuity traces as edges that significantly differ from the model mean surface.

Figure 6: Example of a (a) convex and a (b) concave edge.

At this point, the aim is to determine which vertices are potentially pertaining to edges that are significant: among those vertices the algorithms will choose the vertices to connect to define the edge

paths. So, the second step is the selection of two threshold values, one for maximum principal curvature, called  $T_{\max}$ , and the other for minimum principal curvature, called  $T_{\min}$ . Each vertex of the mesh has a maximum and a minimum principal curvature value; if one of these values is greater (in absolute value) than the respective threshold, the vertex is allowed to be connected to the other significant vertices to create an edge. Decreasing the threshold's absolute values means that more vertices are considered as possible parts of traces (Figure 7 and 8). Therefore, different thresholds can lead to a different number of detected traces and/or traces of different length. There could be two possible strategies for the choice of the thresholds: an automatic one, based on some statistical criteria on curvature values, and a manual one, in which an operator is given some instruments to decide. The choice is not simple, since the optimum threshold can be defined as the curvature value which allows one to satisfy two requirements:

1. To remove all vertices not belonging to any edge;
2. To optimize, for each edge, the number of vertices among which the algorithms will perform the following linking procedure.

Whereas on the one hand it is quite easy to find a value that meets the first requirement, it is, on the other hand, more complex to find a value that meets the second one. In fact, generally edges in the same object can vary depending on their shape and their position. Therefore vertices belonging to the same edge could have different principal curvature values, varying within a certain range; moreover different edges could have, in general, different principal curvature ranges. These are the reasons that led the authors towards a manual choice: the user, by means of colorbars and images, can iteratively choose a threshold value  $T_{\max}$  and see what will be the accepted vertices to create convex edges, operating directly a manual optimization procedure. Then the procedure will be repeated to choose  $T_{\min}$

(in general different in absolute value from  $T_{\max}$ ), to create concave edges. This operation is the only one subject to the user's decision.

Figure 7: Threshold  $T_{\max}$  on maximum principal curvature values allows one to extract convex edges. Number of accepted vertices (black) changes with threshold: (a)  $T_{\max} = 0.1$  (b)  $T_{\max} = 1$ . A higher value of  $T_{\max}$  corresponds to a smaller number of accepted vertices, namely a thinner band along the edges.

Figure 8: Threshold  $T_{\min}$  on minimum principal curvature values allows one to extract concave edges. The number of accepted vertices (black) changes with threshold: (a)  $T_{\min} = -0.1$  (b)  $T_{\min} = -1$ . A higher absolute value of  $T_{\min}$  corresponds to a smaller number of accepted vertices, namely a thinner band along the edges.

Then the connection of vertices is performed with algorithms, developed by Umili (2011), which use information about principal curvature values and principal curvature directions to automatically create edge paths along vertices. The paths are then segmented with the RANSAC algorithm (Fischler and Bolles, 1981): for each path the lines that better interpolate it are obtained and used to split the path according to their different directions (Figure 9). Operating in 3D space, a line is defined as (Equation 1):

$$\begin{cases} X = X_0 + l \cdot t \\ Y = Y_0 + m \cdot t \\ Z = Z_0 + n \cdot t \end{cases} \quad [1]$$

where  $(X_0, Y_0, Z_0)$  is a point of the line,  $(l, m, n)$  are the parameters related to the slope along the 3 directions and  $t$  is an independent variable.

Figure 9: Path segmentation with RANSAC algorithm; example of a path interpolated by 3 different lines and split in 3 parts; each part can be approximated by a segment.

At the end of this procedure, a certain number of paths, that will be called *edges* in the following, and their interpolating segments are stored. Each edge is a list of vertices and each segment is described using the 6 parameters ( $X_0$ ,  $Y_0$ ,  $Z_0$ ,  $l$ ,  $m$ ,  $n$ ).

After that, the ISODATA algorithm (Ball and Hall, 1965) is used to perform automatic cluster analysis, in order to partition the obtained segments into  $k$  clusters (Figure 10); the main advantage of this algorithm, with respect to other methods (i.e. k-means, tree-clustering) based on distance between elements, is that it does not require the exact number of clusters as input. In fact, during the iterations, temporary clusters created using criteria based on distances between elements, can be merged or split according to other criteria (e.g. number of members (segments), distance between centers of clusters, cluster standard deviation), automatically adjusting the number of clusters.

Therefore each final edge is composed of a path connecting a certain number of DSM vertices, its interpolating segment and the cluster to which it belongs.

Figure 10: DSM stairs: edges have been correctly classified into 3 clusters: edges along X ( $K_1$ ), edges along Z ( $K_2$ ), edges along Y ( $K_3$ ); each edge is colored depending on the cluster to which it belongs.

#### **4. Trace sampling**

After the automatic edge identification, a dataset of discontinuity traces is available for further investigations, such as sampling and detailed measurements. Therefore two trace sampling procedures have been implemented to operate on the dataset: the method proposed by Zhang and Einstein (1998),

based on circular window sampling, and the method proposed by Mauldon et al. (2001), based on circular scanline sampling.

The implemented procedure is based on the following idea: edges, which are assumed to represent discontinuity traces in the 3D space, need to be sampled in a 2D window/scanline, therefore they need to be projected on the same plane in which the window/scanline is created. This plane, called “sampling plane” ( $\pi_c$ ), is calculated as the rock mass mean front. Each edge is then an orthogonally projected, which transforms the edge into a polyline in the sampling plane (Figure 11).

Figure 11: Example of an edge projected on sampling plane  $\pi_c$ ; also DSM boundary vertices and possible holes are projected.

Also boundary vertices of the DSM are projected on the plane, creating a contour of the DSM (Figure 11); in case holes are present in the DSM surface, also boundaries of them are projected on the plane. As suggested by Mauldon et al. (2001), a regular grid of centers that are contained within the whole contour is created on the plane (Figure 12) and different radius values are used. Each one of the  $N_n$  nodes of the grid will be the center of  $N_w$  concentric circles with different radius values (Figure 13): in all,  $N_n \cdot N_w$  circular windows/scanlines are created. The maximum circle radius is automatically calculated: considering the sampling plane (e.g.  $\pi_c \equiv XY$ ), the maximum dimensions of the area within the contour can be measured along 2 axes (e.g.  $D_x, D_y$ ). The maximum diameter will be equal to the minimum dimension (e.g. if  $D_x = 10\text{m}$ ,  $D_y = 5\text{m}$  then the maximum radius will be 2.5 m). So it is possible to automatically create windows of different radii, e.g. fixed percentages of the maximum radius. A condition is also checked for each circle: if it is completely within the contour, as suggested by Mauldon et al. (2001), and it does not include DSM hole boundaries, it will be used to perform the sampling, otherwise not (Figure 13).

Figure 12: Creation of the grid and calculation of maximum radius  $c$ .

Figure 13: Creation of concentric windows/scanlines of different radii. Dotted circle 1 will not be used in sampling procedure because it is not completely within the boundary; dotted circle 2 will not be used because it contains a hole.

Figure 14: Traces, i.e. mapped projected edges on sampling plane, are sampled using circular windows/scanlines.

#### 4.1. Sampling methods

The circular window sampling method (Zhang and Einstein, 1998) allows one to calculate the mean trace length, expected discontinuity diameter and intensity of rock discontinuities. The trace sampling procedure is based on a classification of the traces that are visible on the considered sampling window (Figure 15); the lengths of observed traces and the distribution of trace lengths are not required. The major advantage of the proposed method is that it does not need sampling data about the orientation of discontinuities, i.e., the proposed method is applicable to traces with arbitrary orientation distributions: the orientation distribution-free nature of the proposed method comes from the symmetric properties of the circular sampling windows. Therefore, the proposed method can be used to estimate the mean trace length of more than one set of discontinuities.

For each window (Figure 15), traces are classified in the following categories: traces with both ends outside the window ( $N_0$ ), traces with both ends within the window ( $N_2$ ) and traces with only one end within the window ( $N_1$ ). From the sampling on a window of radius  $c$  it is possible to obtain traces samples (called  $\hat{N}_0, \hat{N}_1, \hat{N}_2$ ) to estimate a value for mean trace length  $\mu$  ( $\hat{\mu}$ ) (Equation 2); the total number  $\hat{N}$  of considered traces in a window is the sum of  $\hat{N}_0, \hat{N}_1$  and  $\hat{N}_2$ .

$$\hat{\mu} = \frac{(\hat{N} + \hat{N}_0 - \hat{N}_2)}{(\hat{N} - \hat{N}_0 + \hat{N}_2)} c \quad [2]$$

Figure 15: Classification of traces visible on a sampling window, laying on the sampling plane  $\pi_c$ : type  $N_0$  (dark grey),  $N_1$  (light grey) and  $N_2$  (grey) with respect to the considered window. Dashed traces will not be sampled because they cannot be classified.

The following two special cases should be avoided:

1. If  $\hat{N}_0 = \hat{N}$ , then  $\hat{N}_2 = 0$  and  $\hat{\mu} \rightarrow \infty$ . In this case, all the discontinuities intersecting the sampling window have both ends censored and the denominator of Equation 2 is 0. This implies that the area of the window used for the discontinuity survey may be too small and therefore not representative of the rock mass. To avoid this problem it is necessary to increase window radius.
2. If  $\hat{N}_2 = \hat{N}$ , then  $\hat{N}_0 = 0$  and  $\hat{\mu} = 0$ . In this case, all the discontinuities intersecting the sampling window have both ends observable and the numerator of Equation 2 is 0. To avoid this problem it is necessary to decrease window radius.

In practice, the exact values of  $N$ ,  $N_0$  and  $N_2$  are not known and thus  $\mu$  has to be estimated using sampled data. In other words, the  $\hat{\mu}$  of several sampling windows can be used to evaluate  $\mu$ . Zhang and Einstein (1998) show how the effect of non-uniformity of trace distribution on an outcrop is decreased by averaging. Therefore, they recommend that, in practical sampling, multiple windows of the same size and at different locations should be used. This is the reason why an algorithm to create a large number of windows has been implemented. Figure 16 shows an example: there is a grid consisting of 6 window centers and for each one there are 4 concentric windows of different radius (1-2-3-4 m). In the following, parameters will be shown in relation to the window radius: actually, mean values will be shown, calculated from all the windows with a certain radius. So, for a radius equal to 1 m, the

resulting value of the mean trace length  $\mu$  from Figure 16 is calculated as the mean of the values obtained from the 6 considered windows with radius 1 m.

Figure 16: Example of regular grid composed by 6 nodes; each one is center of 4 circular windows with different radius values.

The circular scanline sampling method (Mauldon et al., 2001) allows one to calculate mean trace length, trace density and trace intensity, parameters that measure fracture size and abundance. The trace sampling procedure is based on a classification of the traces with respect to the circular scanline (Figure 17); the lengths of observed traces and the distribution of trace lengths are not required.

For each window it is necessary to count the number  $n$  of traces intersecting the circular scanline and the number  $m$  of trace end points within the circular area delimited by the scanline. From each scanline sampled  $\hat{n}$  and  $\hat{m}$  can be obtained and used to estimate  $\hat{\mu}$  (Equation 3).

$$\hat{\mu} = \frac{\pi \cdot c}{2} \left( \frac{\hat{n}}{\hat{m}} \right) \quad [3]$$

Figure 17: Classification of traces points:  $n$  traces intersecting *scanline* (grey);  $m$  traces end points within circular area (black).

## 4.2. Parameters definition

The parameters used in the following are defined first:

- Mean trace length  $\mu$ : this parameter is defined as the mean of the true trace length distribution  $f(l)$  (i.e. the trace length distribution on an infinite sampling surface). It is calculated using Equation 2, proposed by Zhang and Einstein (1998), based on the count of traces classified



according to their position with respect to the circular window, or Equation 3, proposed by Mauldon et al. (2001), based on the count of nodes that represents traces end points and intersections between a trace and the circular scanline.

- Expected discontinuity diameter  $E(D)$ : this parameter is defined as the mean of the discontinuity diameter distribution  $g(D)$ , whose form is assumed choosing among lognormal, negative exponential and Gamma. The best distribution of  $g(D)$  is chosen using a test proposed by Zhang and Einstein (2000) and it can be different from the trace length distribution  $f(l)$  form. These authors propose a different expression for  $E(D)$  for each of the three distribution forms.
- Intensity of rock discontinuities  $P_{32}$ : the adopted measure to express the intensity of rock discontinuities is  $P_{32}$ , fracture area per unit volume. Zhang and Einstein (2000) proposed to calculate the mean fracture area per unit volume of the rock mass as:

$$P_{32} = \frac{N_t \cdot E(A)}{V} \quad [4]$$

where  $N_T$  is the total number of sampled discontinuities in a window,  $E(A)$  is the mean discontinuity area calculated with the equation:

$$E(A) = \int_0^{\infty} \frac{\pi}{4} D^2 g(D) dD = \frac{\pi}{4} E(D^2) = \frac{\pi}{4} [(\mu_D)^2 + (\sigma_D)^2] \quad [5]$$

and  $V$  is the unit volume, here considered as a cylinder:

$$V = \pi c^2 h \quad [6]$$

where  $c$  is the radius of the considered sampling window and  $h$  is the cylinder depth. Two values of  $h$  have been used here: 1m (fixed for all windows) and a value equal to the relative window radius  $c$  (varying with the windows dimensions).

## 5. Comparison of two sampling methods on a case study

The new trace detection and mapping method proposed here has been applied in a case study, the North face of the Aiguilles du Marbrées (Mont Blanc), on which also the manual trace detection method was performed (Ferrero and Umili, 2011). At this site a close-range photogrammetric survey was performed; after photogrammetric data processing an orthophotograph and a DSM of the rock face were created. Manual trace detection and circular window sampling was performed on the orthophotograph of the rock mass (Figure 18). Four centers were placed on the image and, for each one, five radius values were used to draw sampling windows. So 20 sampling windows were used to calculate the final parameter values (Figure 19).

Figure 18: Orthophotograph (base 90 m, height 60 m) with mapped traces.

Figure 19: Mapped traces are sampled using 20 circular windows.

Then the DSM of Aiguille du Marbree, representing the same part of the rock mass shown in the orthophotograph, but with smaller dimensions (Figure 20), was used as input data for the new method; this is a high resolution DSM (approximately 50 pts/m<sup>2</sup>).

Figure 20: a) Orthophotograph, b) DSM (base 62 m, height 52 m, 163963 vertices); white rectangular window on the left is common portion of rock mass between 2D orthophotograph and 3D model.

Three curvature threshold couples ( $T_{\max}$ ,  $T_{\min}$ ) were used to detect traces on the DSM to check if significant variations of detected traces and parameter values could occur when varying the thresholds.

Comparing the traces detected in the three different cases (Figure 21) it is possible to notice small variations of trace lengths and an increasing number of traces when thresholds decrease, as expected. Comparing the detected traces obtained with the two methods, one can see that sub-horizontal traces detected in the orthophotograph are longer and their number is greater than in the DSM (Figure 18 and 21). This can be due to three different reasons: the first one is that traces were actually longer but the automatic detection process did not produce a complete result. In fact, the density of the DSM vertices could have been not sufficient to clearly define sub-horizontal edges and so curvature values in these surface areas do not have the correct curvature range. Another possibility is that the chosen curvature thresholds were not suitable to completely detect traces (e.g. thresholds were too high and many vertices were not allowed to be part of the edges). The third reason could instead be that the operator, during the manual sampling on the orthophotograph, connected different portions of traces that were not actually connected in the real rock mass, due to perspective distortion and to occlusions. Also, he could have detected “false” traces, due to rock color or shadows.

2500 centers were placed on a regular grid on the sampling plane and, for each one, nine radius values were used to automatically draw sampling windows and to perform the sampling procedure.

Figure 21: DSM (base 62 m, height 52 m); traces are detected using three different combinations of thresholds  $[T_{\max}; T_{\min}]$  a)  $T_1=[0.9; -0.7]$ , b)  $T_2=[0.8; -0.6]$ , c)  $T_3=[0.7; -0.5]$ .

One of the main advantages of the automatic method is the opportunity to have a very large number of sampling windows analyzed in a short time. Table 1 shows the numbers of windows, classified in 3 radius ranges, used for the manual sampling on the orthophotograph and the automatic sampling on the DSM, performed on circular windows and circular scanlines; discarded windows (e.g. windows partially outside the boundary) are not included. Manual and automatic trace detection needed both about 2 hours; considering only the sampling procedure, the time needed for manual sampling on the

orthophotograph was about 5 hours (about 15 minutes for each one of the windows), while the time needed for automatic sampling on the DSM was about 2-3 hours (about 2 seconds for each of the windows/scanlines) using an Intel 2.8GHz workstation.

Table 1: Number of windows used to calculate parameters with manual method on an orthophoto and with automatic methods on DSM (circular window/scanline, 3 different threshold couples  $T_1, T_2, T_3$ ).

	Sampling Method		N° of used windows/scanlines		
	procedure	tool	0-10 m	10-20 m	20-30 m
<b>orthophoto</b>	manual	window	8	12	0
<b>DSM T1</b>	automatic	window	1205	1191	165
<b>DSM T2</b>	automatic	window	1435	1230	169
<b>DSM T3</b>	automatic	window	1597	1282	170
<b>DSM T1</b>	automatic	scanline	3669	1323	170

From the data obtained during the window sampling procedure on the DSM, the previously described parameters (mean trace length  $\mu_l$ , expected discontinuity diameter  $E(D)$  and intensity of rock discontinuity  $P_{32}$ ) have been automatically calculated using Zhang's and Einstein's (1998, 2000) equations and were compared to those obtained from the orthophotograph. Mean trace lengths were calculated from data obtained considering circular scanlines only using Mauldon's et al. (2001) equation, and were compared to results obtained using Zhang's and Einstein's (1998) equation.

Figure 22 shows the comparison between the values of mean trace lengths  $\mu_l$  obtained with varying window radius  $c$ . The orthophoto results are on average 1 m lower than DSM results, but the trends are similar. The three DSM trends have a maximum difference of about 0.6 m for the maximum radius; it is interesting to notice that in this case the smaller thresholds couple ( $T_3$ ) produces smaller values than  $T_2$ . This fact could be the proof that, once the actual amount of traces is recognized and the corresponding  $\mu$  value is obtained, even decreasing the curvature thresholds and so allowing more

vertices to be part of a trace will not increase the mean trace length beyond this value. However, this fact must be further investigated.

Figure 22: Mean trace length calculated according to Zhang and Einstein (1998) from data sampled on orthophoto and on DSM (3 threshold couples).

Figure 23 shows the comparison between orthophoto and DSM trends of expected discontinuity diameter  $E(D)$  when varying window radius  $c$ . The three DSM trends are similar and their maximum difference is less than 0.2 m. The difference between orthophoto and DSM trends decreases when increasing the radius and they intersect for a radius of about 18 m (that is the maximum radius used in manual sampling). This fact is quite interesting and it suggests that it is important to use large radius values to be sure to obtain data that are representative of the rock mass.

Figure 23: Expected discontinuity diameter calculated according to Zhang and Einstein (2000) from data sampled on orthophoto and on DSM (3 threshold couples).

Figure 24 shows the comparison between orthophoto and DSM trends of the intensity of rock discontinuities  $P_{32}$ , calculated with a cylindrical volume whose base is equal to the windows area and whose depth  $h$  is equal to 1 m, with varying window radius. The three DSM trends are similar and their maximum difference is about  $0.22 \text{ m}^{-1}$ . Similar to Figure 23, the difference between orthophoto and DSM trends decreases when increasing the radius and they intersect for a radius of about 12-15 m.

Figure 24: Intensity of rock discontinuities calculated according to Zhang and Einstein (2000) from data sampled on orthophoto and on DSM (3 threshold couples); cylinder volume depth is equal to 1m.

Figure 25 shows the comparison between orthophoto and DSM trends of the intensity of rock discontinuities  $P_{32}$ , calculated with a cylindrical volume whose base is equal to the windows area and whose depth  $h$  is equal to the radius  $c$  with varying window radius. The trends are similar to a negative

exponential function but with different coefficients. This way of calculating  $P_{32}$  could be used to define an analytical relation between  $P_{32}$  and window radius, that could be easily introduced in a rock mass fracture model.

Figure 25: intensity of rock discontinuity calculated according to Zhang and Einstein (2000) from data sampled on orthophoto and on DSM (3 threshold couples); cylinder volume depth is equal to radius  $c$ .

Figure 26 shows the comparison between the values of mean trace lengths  $\mu_1$  obtained with circular window (Zhang and Einstein, 1998) and scanline (Mauldon et al., 2001) sampling with varying window radius  $c$ ; sampling has been performed on the traces detected using threshold couple  $T_1$ . The window method (ZE) trend is on average 0.5 m lower than scanline (MDR) trend, but they are similar.

Figure 26: Mean trace length calculated according to Zhang and Einstein (1998) and Mauldon et al. (2001) from data sampled on DSM (threshold couple  $T_1$ ).

## 6. Conclusions

The intensity of discontinuities in a rock mass depends on the areas of the discontinuities, which usually cannot be measured. However, they can be estimated on the basis of the discontinuity trace length and the expected diameter. The mean trace length can be evaluated in a statistical way and two different proposed approaches are compared in this paper; also the expected diameter can be evaluated in a statistical way. However the soundness of this kind of estimation is based on a reliable sampling method.

For this reason a new automatic approach is proposed in this work, which is based on trace mapping and sampling on a DSM. Compared to manual trace sampling on an image (e.g. an orthophoto), it allows one to quickly perform sampling on a very large number of windows for different locations on the rock face and with different radii. Moreover, it has the great advantage of using only geometric

information, without need to interpret colors and shades. In this way colors have no influence on the choice of what is a trace or not and results are less affected by false traces. This method requires only the input DSM and two thresholds on principal curvature values, then all the operations are automatically performed. The results depend on the quality of the DSM (point cloud density, *noise*, possible holes in the surface).

At present, considering the obtained results, it is possible to observe that parameter values and trends from orthophoto and DSM sampled data are different, but for larger radius values the differences decrease: this is very important, especially to prove that the new method can be a useful tool to quickly obtain order of magnitude of parameters values.

However this approach raises a new issue, that is the way to decide which curvature threshold couple is best suited to map traces. Considering the similarity of parameter trends (Fig. 22-23-24-25) obtained from DSM data using 3 different curvature threshold couples (Fig. 21), the suggestion could be to define a range of threshold values that allow one to correctly map traces; then it would be possible to define the corresponding range of parameters trends and evaluate its reliability. Anyway, this work can be considered as an initial investigation; the method should eventually be tested on some other DSMs in order to make comparisons of results.

Ball, G.H., Hall, D.J., 1965. ISODATA, A novel method of data analysis and pattern classification. Stanford Research Institute, Menlo Park, CA, Technical Report AD 699616, 61pp.

Baltsavias, E.P., 1999. A comparison between photogrammetry and laser scanning. ISPRS. Journal of Photogrammetry & Remote Sensing 54 (2-3): 83-94.

Barrow, H.G., Tenenbaum, J.M., 1981. Interpreting line drawings as three-dimensional surfaces. Artificial Intelligence 17: 75-116.

- Canny, J., 1986. A Computational Approach to Edge Detection. *IEEE Transactions on Pattern Analysis and Machine Intelligence* 8(6): 679-698.
- Chen, X., Schmitt, F., 1992. Intrinsic Surface Properties from Surface Triangulation. *Proceedings of the European Conference on Computer Vision*, pp. 739-743.
- Cravero, M., Iabichino, G., 1992. Caratterizzazione e modellazione geometrica dei campi di fratture naturali. Published in: *IV Ciclo di Conferenze di Meccanica e Ingegneria delle Rocce su "Previsioni e riscontri"* (p. 6.1- 6.60), Torino [in Italian].
- Dershowitz, W., 1979. Jointed Rock Mass Deformability. M.S. Thesis. Massachusetts Institute of Technology, MA. 292 pp.
- Dershowitz, W.S., Einstein, H.H., 1988. Characterizing rock joint geometry with joint system models. *Rock Mechanics and Rock Engineering* 21: 21-51.
- Dong, C., Wang, G., 2005. Curvatures estimation on triangular mesh. *Journal of Zhejiang University SCIENCE* 6A(Suppl I): 128-136.
- Euler, L., 1760. Recherches sur la courbure des surfaces, *Memoires de l'academie des sciences de Berlin* 16, 1767: 119–143, 1767, <http://math.dartmouth.edu/~euler/pages/E333.html>.
- Feng, Q., Roshoff, K., 2006. Semi-automatic mapping of discontinuity orientation at rock exposure by using 3D laser scanning techniques. The 10th IAEG International Congress, Nottingham, UK. Paper number 751.
- Ferrero, A., Forlani, G., Roncella, R., Voyat, H., 2009. Advanced geostructural survey methods applied to rock mass characterization. *Rock Mechanics and Rock Engineering* 42: 631-665.
- Ferrero, A., Umili, G., 2011. Comparison of Methods for Estimating Fracture Size and Intensity: Aiguille du Marbrée (Mont Blanc). *International Journal of Rock Mechanics and Mining Sciences* 48: 1262-1270.



- Fischler, M., Bolles, R., 1981. Random sample consensus: a paradigm for model fitting with application to image analysis and automated cartography. *Communications of the Association for Computing Machinery*, 24(6): 381-395.
- Gigli, G., Casagli, N., 2011. Semi-automatic extraction of rock mass structural data from high resolution LIDAR point clouds. *International Journal of Rock Mechanics and Mining Sciences* 48(2): 187-198.
- Haneberg, W.C., 2006. 3-D rock mass characterization using terrestrial digital photogrammetry. *AEG News* 49:12–5.
- ISRM, 1978. Commission on standardization of laboratory and field tests. Suggested methods for the quantitative description of discontinuities in rock masses. *International Journal of Rock Mechanics and Mining Sciences and Geomechanics Abstracts* 15, 319–368.
- Kemeny, J., Donovan, J., 2005. Rock mass characterization using LiDAR and automated point cloud processing. *Ground Engineering* 38 (11): 26-29.
- Kemeny, J., Post, R., 2003. Estimating three-dimensional rock discontinuity orientation from digital images of fracture traces. *Computers and Geosciences* 29: 65–77.
- Kraus, K., 1993. *Photogrammetry*, vol 1, 4th edn. In: Dummler F (ed), Bonn. ISBN:3-427-78684-6.
- Kraus, K., Pfeifer, N., 1998. Determination of terrain models in wooded areas with airborne laser scanner data. *ISPRS Journal of Photogrammetry & Remote Sensing*, 53 (4): 193–203.
- Kulatilake, P.H.S.W., Wu, T.H., 1984. Estimation of mean trace length of discontinuities. *Rock Mechanics and Rock Engineering* 17: 215-232.
- Lato, M.J., Diederichs, M.S., Hutchinson, D.J., Harrap, R., 2012. Evaluating roadside rockmasses for rockfall hazards using LiDAR data: optimizing data collection and processing protocols. *Natural Hazards* 60(3): 831-864.

Lemy, F., Hadjigeorgiou, J., 2003. Discontinuity trace map construction using photographs of rock exposures. *International Journal of Rock Mechanics and Mining Sciences* 40: 903–917.

Lindeberg, T., 2001. Edge detection, in M. Hazewinkel (editor), *Encyclopedia of Mathematics*, Kluwer/Springer, ISBN 1402006098.

Maerz, N.H., 1990. Photoanalysis of rock fabric. PhD Dissertation, University of Waterloo, Canada, 227 pp.

Mauldon, M., Dunne, W.M., Rohrbaugh, M.B.Jr., 2001. Circular scanlines and circular windows: new tools for characterizing the geometry of fracture traces. *Journal of Structural Geology* 23: 247-258.

Mauldon, M., 1998. Estimating Mean Fracture Trace length and Density from Observations in Convex Windows. *Rock Mechanics and Rock Engineering* 31 (4): 201-216.

Post, R., Kemeny, J., Murphy, R., 2001. Image processing for automatic extraction of rockjoint orientation data from digital images. *Proceedings of the 38th US Rock Mechanics Symposium*, Washington, DC. A.A. Balkema, Rotterdam, pp. 877–884.

Reid, T.R., Harrison, J.P., 2000. A semi-automated methodology for discontinuity trace detection in digital images of rock mass exposures. *International Journal of Rock Mechanics and Mining Sciences* 37: 1073-1089.

Rohrbaugh, M.B.Jr., Dunne, W.M., Mauldon, M., 2002. Estimating fracture trace intensity, density and mean length using circular scan lines and windows. *The American Association of Petroleum Geologist*, vol. 86, no. 12, pp. 2089-2104.

Roncella, R., Forlani, G., 2005. Extraction of planar patches from point clouds to retrieve dip and dip direction of rock discontinuities. *ISPRS WG III/3, III/4, V/3 Workshop ‘Laser scanning 2005’* Enschede.

- Slob, S., Hack, H.R.G.K., Feng, Q., Röshoff, K., Turner, A.K., 2007. Fracture mapping using 3D laser scanning techniques. Proceedings of the 11th congress of the International Society for Rock Mechanics, Lisbon, Portugal. Vol. 1. pp. 299-302.
- Sturzenegger, M., Stead, D., 2009. Close-range terrestrial digital photogrammetry and terrestrial laser scanning for discontinuity characterization on rock cuts. *Engineering Geology* 106: 163–182.
- Trinks, I., Clegg, P., McCaffrey, K., Jones, R., Hobbs, R., Holdsworth, B., 2005. Mapping and analyzing virtual outcrops. *Visual Geosciences* 10: 13–19.
- Umili, G., 2011. Ricostruzione automatica delle linee di rottura nei Modelli Digitali di Superficie con applicazioni in ambito geotecnico e architettonico. PhD Dissertation, University of Parma, 127 pp. [in Italian]
- Wu, H., Pollard, D.D., 1995. An experimental study of the relationship between joint spacing and layer thickness. *Journal of Structural Geology* 17(6): 887-905.
- Zhang, L., Einstein, H.H., 1998. Estimating the Mean Trace Length of Rock Discontinuities. *Rock Mechanics and Rock Engineering* 31 (4): 217-235.
- Zhang, L., Einstein, H.H., 2000. Estimating the intensity of rock discontinuities. *International Journal of Rock Mechanics and Mining Sciences* 37: 819-837.

### Image list:

Figure 1: Detail of a shaded surface portion of a Digital Surface Model (DSM), representing discontinuity planes separated by convex and concave edges.

Figure 2: Triangulated vertices which constitute portion of DSM in Fig.1; a) high resolution DSM produces a better representation of edges than b) low resolution.

Figure 3: Example of convex and concave edges detected on test-object: DSM stairs is composed by 116601 points and 231909 triangles.

Figure 4: Definition of principal curvature of a vertex  $P$  of a surface requires definition of normal  $N$  and normal plane  $\pi$ . a) Plane  $\pi_1$  generates a curve  $C_1$  whose osculating circle in  $P$  has a radius  $r_1$ ; b) plane  $\pi_2$  is obtained rotating  $\pi_1$  about the normal  $N$ ; it generates a curve  $C_2$  whose osculating circle in  $P$  has a radius  $r_2$  greater than  $r_1$ .

Figure 5: a) One-ring neighborhood of vertex  $P$  is formed by all the triangles that contain  $P$ ; b) two-ring neighborhood of  $P$  is composed by one-ring triangles and triangles that contain at least 1 vertex belonging to one-ring neighborhood.

Figure 6: Example of a (a) convex and a (b) concave edge.

Figure 7: Threshold  $T_{\max}$  on maximum principal curvature values allows one to extract convex edges. Number of accepted vertices (black) changes with threshold: (a)  $T_{\max} = 0.1$  (b)  $T_{\max} = 1$ . A higher value of  $T_{\max}$  corresponds to a smaller number of accepted vertices, namely a thinner band along the edges.

Figure 8: Threshold  $T_{\min}$  on minimum principal curvature values allows one to extract concave edges. The number of accepted vertices (black) changes with threshold: (a)  $T_{\min} = -0.1$  (b)  $T_{\min} = -1$ . A higher

absolute value of  $T_{\min}$  corresponds to a smaller number of accepted vertices, namely a thinner band along the edges.

Figure 9: Path segmentation with RANSAC algorithm; example of a path interpolated by 3 different lines and split in 3 parts; each part can be approximated by a segment.

Figure 10: DSM stairs: edges have been correctly classified into 3 clusters: edges along X ( $K_1$ ), edges along Z ( $K_2$ ), edges along Y ( $K_3$ ); each edge is colored depending on the cluster to which it belongs.

Figure 11: Example of an edge projected on sampling plane  $\pi_c$ ; also DSM boundary vertices and possible holes are projected.

Figure 12: Creation of the grid and calculation of maximum radius  $c$ .

Figure 13: Creation of concentric windows/scanlines of different radii. Dotted circle 1 will not be used in sampling procedure because it is not completely within the boundary; dotted circle 2 will not be used because it contains a hole.

Figure 14: Traces, i.e. mapped projected edges on sampling plane, are sampled using circular windows/scanlines.

Figure 15: Classification of traces visible on a sampling window, laying on the sampling plane  $\pi_c$ : type  $N_0$  (dark grey),  $N_1$  (light grey) and  $N_2$  (grey) with respect to the considered window. Dashed traces will not be sampled because they cannot be classified.

Figure 16: Example of regular grid composed by 6 nodes; each one is center of 4 circular windows with different radius values.

Figure 17: Classification of traces points:  $n$  traces intersecting *scanline* (grey);  $m$  traces end points within circular area (black).

Figure 18: Orthophotograph (base 90 m, height 60 m) with mapped traces.

Figure 19: Mapped traces are sampled using 20 circular windows.

Figure 20: a) Orthophotograph, b) DSM (base 62 m, height 52 m, 163963 vertices); white rectangular window on the left is common portion of rock mass between 2D orthophotograph and 3D model.

Figure 21: DSM (base 62 m, height 52 m); traces are detected using three different combinations of thresholds  $[T_{\max}; T_{\min}]$  a)  $T_1=[0.9; -0.7]$ , b)  $T_2=[0.8; -0.6]$ , c)  $T_3=[0.7; -0.5]$ .

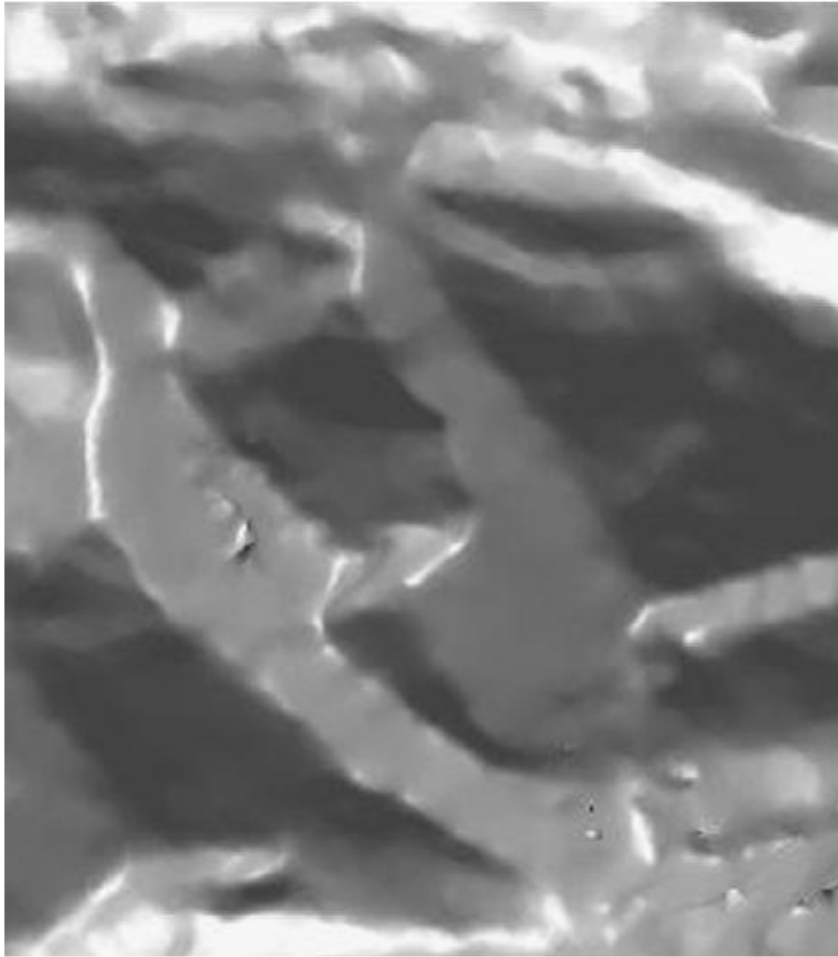
Figure 22: Mean trace length calculated according to Zhang and Einstein (1998) from data sampled on orthophoto and on DSM (3 threshold couples).

Figure 23: Expected discontinuity diameter calculated according to Zhang and Einstein (2000) from data sampled on orthophoto and on DSM (3 threshold couples).

Figure 24: Intensity of rock discontinuities calculated according to Zhang and Einstein (2000) from data sampled on orthophoto and on DSM (3 threshold couples); cylinder volume depth is equal to 1m.

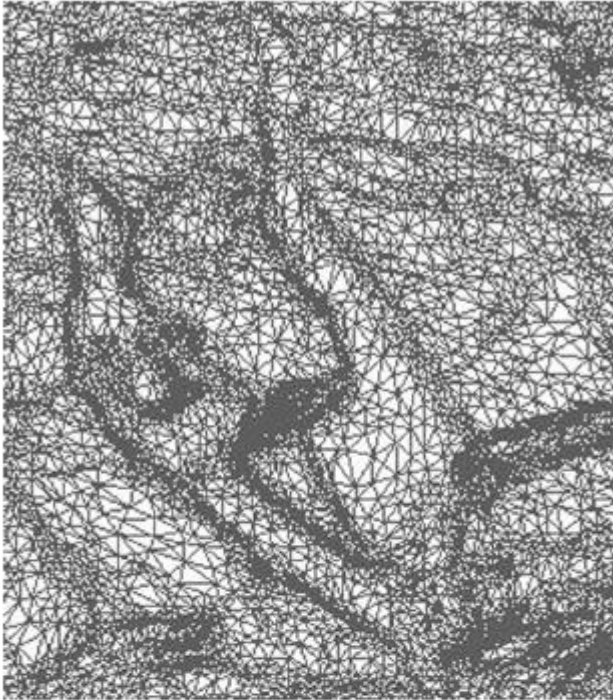
Figure 25: intensity of rock discontinuity calculated according to Zhang and Einstein (2000) from data sampled on orthophoto and on DSM (3 threshold couples); cylinder volume depth is equal to radius  $c$ .

Figure 26: Mean trace length calculated according to Zhang and Einstein (1998) and Mauldon et al. (2001) from data sampled on DSM (threshold couple  $T_1$ ).



**Fig. 1.** Detail of a shaded surface portion of a Digital Surface Model (DSM), representing discontinuity planes separated by convex and concave edges.

a



b

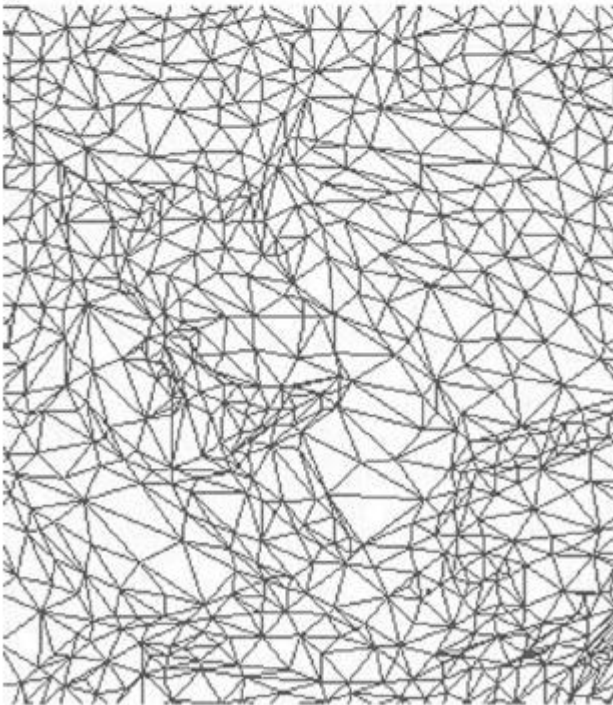


**Fig. 2.** Triangulated vertices which constitute portion of DSM in Fig. 1(a) high resolution DSM produces a better representation of edges than (b) low resolution.



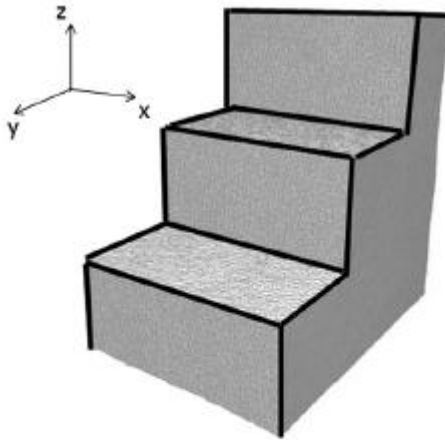


**Fig. 3.** Example of convex and concave edges detected on test-object: DSM stairs is composed by 116601 points and 231909 triangles.

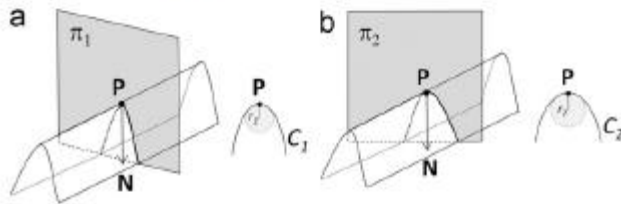


**Fig. 4.** Definition of principal curvature of a vertex  $P$  of a surface requires definition of normal  $N$  and normal plane  $\pi$ . (a) Plane  $\pi_1$  generates a curve  $C_1$  whose osculating circle in  $P$  has a radius  $r_1$ ; (b) plane  $\pi_2$  is obtained rotating  $\pi_1$  about the normal  $N$ ; it generates a curve  $C_2$  whose osculating circle in  $P$  has a radius  $r_2$  greater than  $r_1$ .

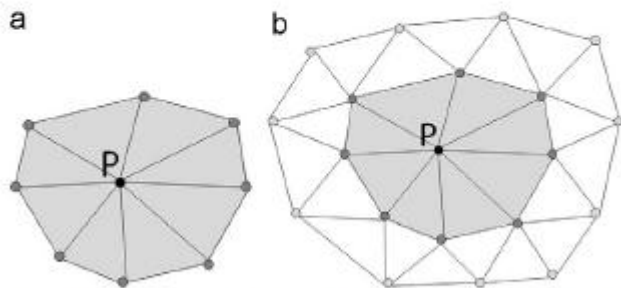


**Fig. 5.** (a) One-ring neighborhood of vertex  $P$  is formed by all the triangles that contain  $P$ ; (b) two-ring neighborhood of  $P$  is composed by one-ring triangles and triangles that contain at least 1 vertex belonging to one-ring neighborhood.

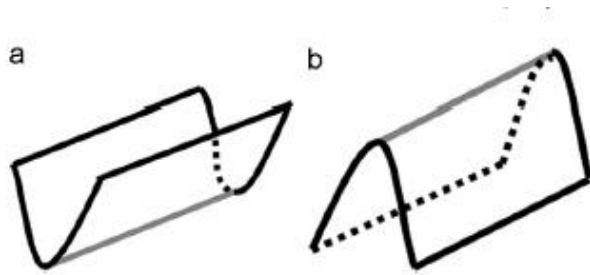


Fig. 6. Example of a (a) convex and a (b) concave edge.

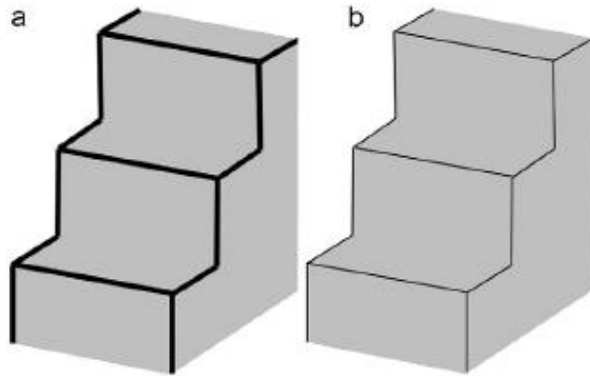


Fig. 7. Threshold  $T_{max}$  on maximum principal curvature values allows one to extract convex edges. Number of accepted vertices (black) changes with threshold: (a)  $T_{max}=0.1$  (b)  $T_{max}=1$ . A higher value of  $T_{max}$  corresponds to a smaller number of accepted vertices, namely a thinner band along the edges.

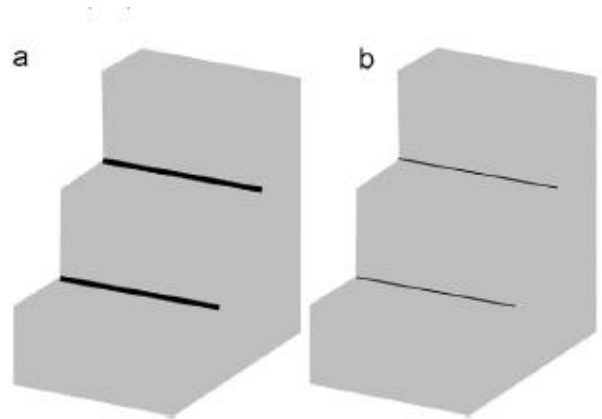


Fig. 8. Threshold  $T_{min}$  on minimum principal curvature values allows one to extract concave edges. The number of accepted vertices (black) changes with threshold: (a)  $T_{min}=-0.1$  (b)  $T_{min}=-1$ . A higher absolute value of  $T_{min}$  corresponds to a smaller number of accepted vertices, namely a thinner band along the edges.

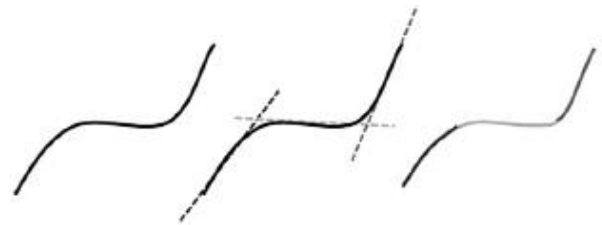
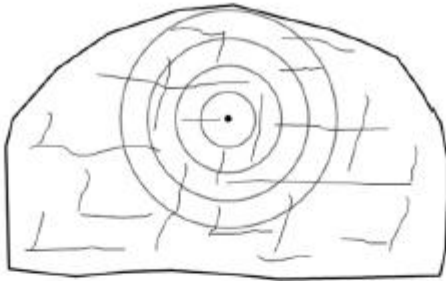
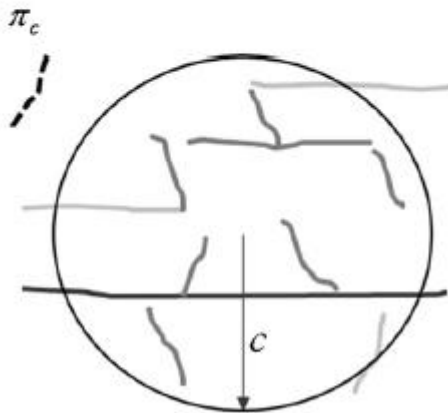


Fig. 9. Path segmentation with RANSAC algorithm; example of a path interpolated by 3 different lines and split in 3 parts; each part can be approximated by a segment.



**Fig. 14.** Traces, i.e., mapped projected edges on sampling plane, are sampled using circular windows/scanlines.



**Fig. 15.** Classification of traces visible on a sampling window, laying on the sampling plane  $\pi_c$ : type  $N_0$  (dark grey),  $N_1$  (light grey) and  $N_2$  (grey) with respect to the considered window. Dashed traces will not be sampled because they cannot be classified.

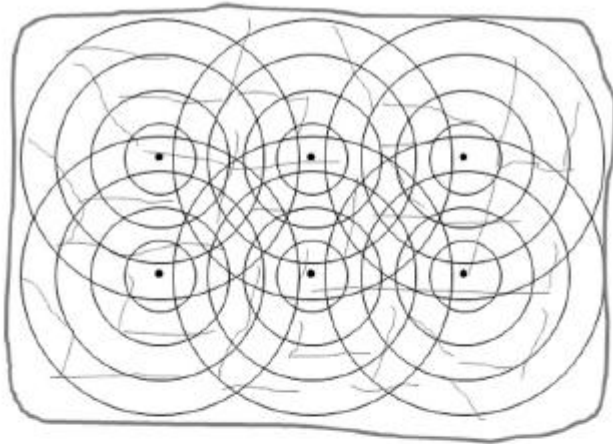


**Fig. 16.** Example of regular grid composed by 6 nodes; each one is center of 4 circular windows with different radius values.

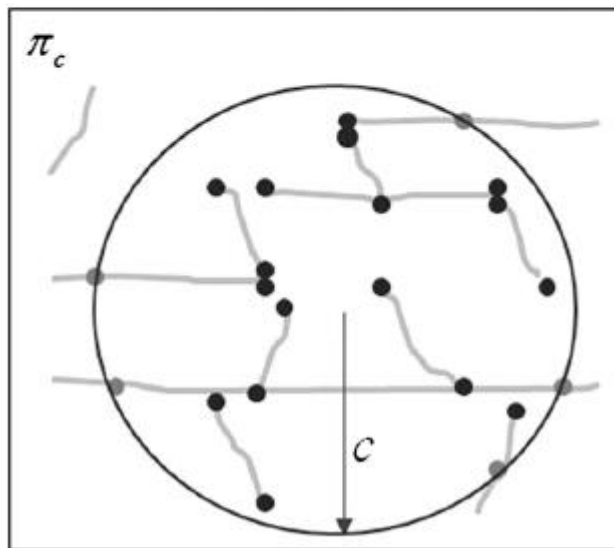


**Fig. 17.** Classification of traces points:  $n$  traces intersecting scanline (grey);  $m$  traces end points within circular area (black).

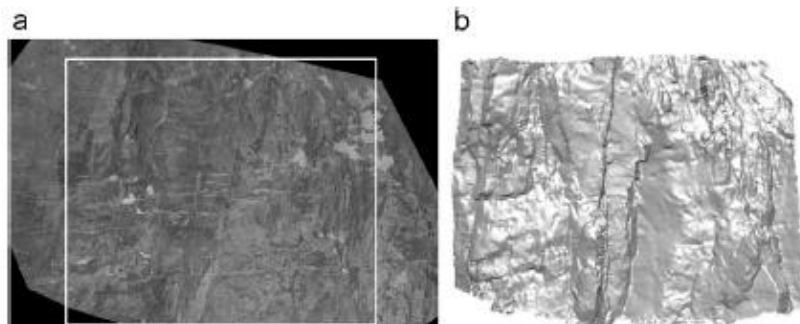


**Fig. 20.** (a) Orthophotograph, (b) DSM (base 62 m, height 52 m, 163963 vertices); white rectangular window on the left is common portion of rock mass between 2D orthophotograph and 3D model.

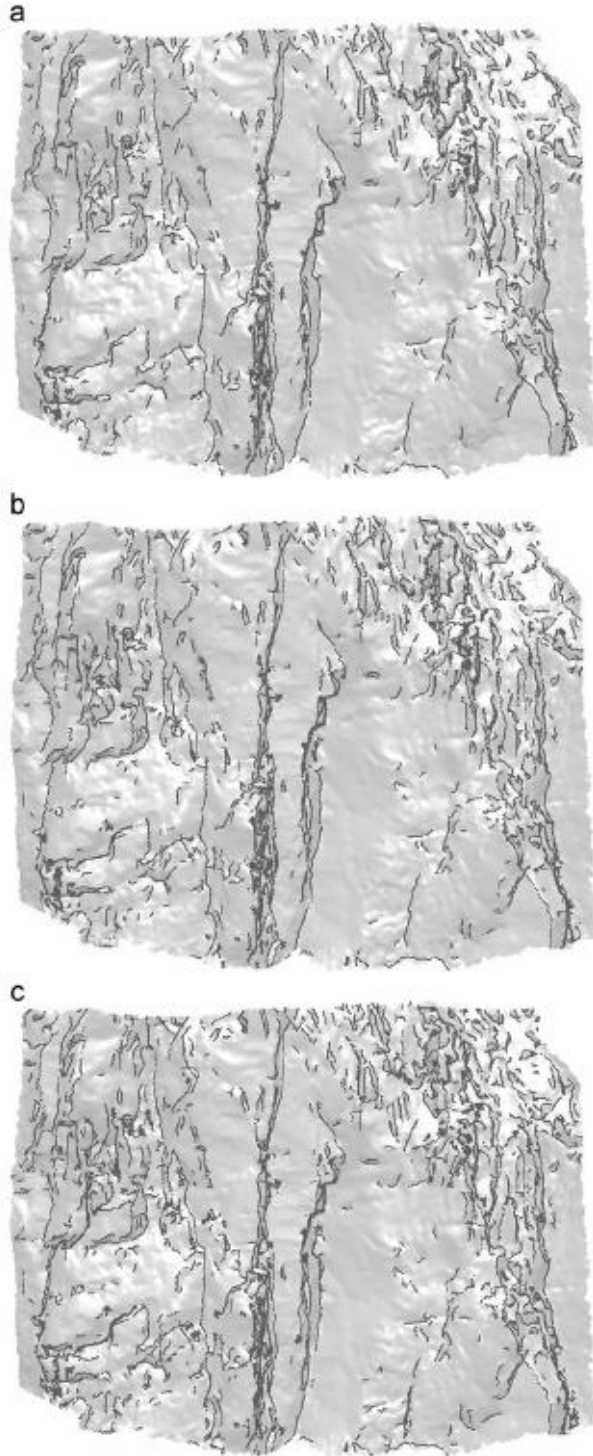


Fig. 21. DSM (base 62 m, height 52 m); traces are detected using three different combinations of thresholds [ $T_{max}; T_{min}$ ] (a)  $T_1 = [0.9; -0.7]$ , (b)  $T_2 = [0.8; -0.6]$ , (c)  $T_3 = [0.7; -0.5]$ .

Table 1

Number of windows used to calculate parameters with manual method on an orthophoto and with automatic methods on DSM (circular window/scanline, 3 different threshold couples  $T_1, T_2, T_3$ ).

	Sampling method		N° of used windows/scanlines		
	Procedure	Tool	0–10 m	10–20 m	20–30 m
Orthophoto	Manual	Window	8	12	0
DSM T1	Automatic	Window	1 205	1 191	165
DSM T2	Automatic	Window	1 435	1 230	169
DSM T3	Automatic	Window	1 597	1 282	170
DSM T1	Automatic	Scanline	3 669	1 323	170

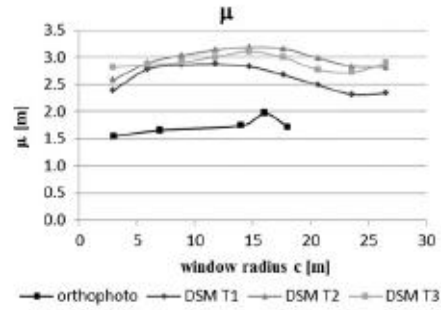


Fig. 22. Mean trace length calculated according to Zhang and Einstein (1998) from data sampled on orthophoto and on DSM (3 threshold couples).

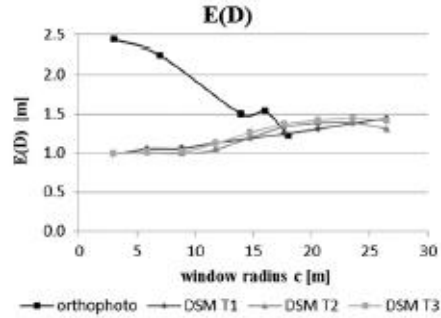


Fig. 23. Expected discontinuity diameter calculated according to Zhang and Einstein (2000) from data sampled on orthophoto and on DSM (3 threshold couples).

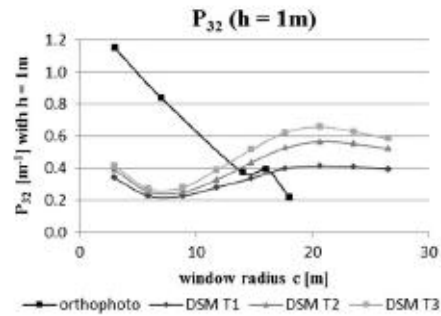


Fig. 24. Intensity of rock discontinuities calculated according to Zhang and Einstein (2000) from data sampled on orthophoto and on DSM (3 threshold couples); cylinder volume depth is equal to 1 m.

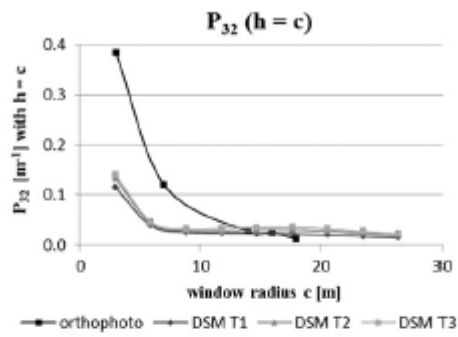


Fig. 25. intensity of rock discontinuity calculated according to Zhang and Einstein (2000) from data sampled on orthophoto and on DSM (3 threshold couples); cylinder volume depth is equal to radius  $c$ .

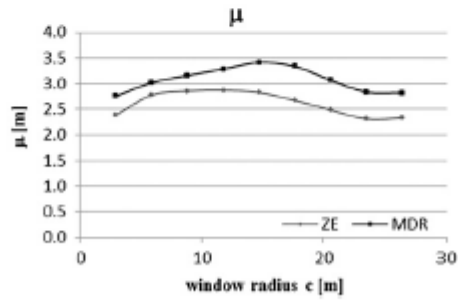


Fig. 26. Mean trace length calculated according to Zhang and Einstein (1998) and Mauldon et al. (2001) from data sampled on DSM (threshold couple  $T_1$ ).